Antithermal quenching and multiparametric temperature sensing from Mn2+/Tb3+-codoped ca2LaTaO6 phosphor

Chen, Yuqi; Li, Guixian; Ding, Yang; Mao, Qinan; Liu, Meijiao; Wang, Chunhua; Zheng, Runtian; Su, Bao-Lian; Zhong, Jiasong

Published in:
Advanced Photonics Research

DOI:
10.1002/adpr.202300106

Publication date:
2023

Document Version
Publisher's PDF, also known as Version of record

ADVANCED PHOTONICS RESEARCH
Open Access
www.adpr-journal.com

Antithermal Quenching and Multiparametric Temperature Sensing from Mn^{2+}/Tb^{3+}-Codoped Ca_2LaTaO_6 Phosphor

Yuqi Chen, Guixian Li, Yang Ding, Qinan Mao, Meijiao Liu, Chunhua Wang, Runtian Zheng, Bao-Lian Su,* and Jiasong Zhong**

Luminescence thermometry plays significant roles in various fields including industrial production, environmental detection, aerospace, and medicine. However, its accuracy improvement remains highly challenging due to the thermal quenching effect of phosphors. Herein, for the first time, a thermal-activated electron compensation Mn^{2+}- and Tb^{3+}-codoped Ca_2LaTaO_6 phosphor is developed for multiparametric temperature sensing with tunable emission of Mn^{2+} and antithermal quenching emission of Tb^{3+}, leading to excellent accuracy at high temperatures. By virtue of the deep electron trap states induced by Mn^{2+} dopant, the electrons in the deep trap can be thermally activated at high temperatures, which can replenish the attenuated Tb^{3+} emission caused by thermal quenching, thus bringing out the antithermal quenching phenomenon. On account of the prominent emission properties, the luminescence intensity ratio (LIR) readout and lifetime-based thermometry are designed, providing a maximum relative sensitivity S_R of 3.603% and 1.941% K^{-1}, respectively. Multiparametric temperature sensing and novel data analysis are also employed to further improve the accuracy of the luminescence thermometer. The outstanding relative thermal sensitivity ranging from 8.72% to 16.11% K^{-1} and temperature uncertainty order of 10^{-3} are achieved. These results demonstrate that the designed Ca_2LaTaO_6:Mn^{2+}/Tb^{3+} phosphor material is a promising thermal-sensing candidate.

1. Introduction

Temperature is at the heart of countless natural and artificial processes such as industrial production, environmental detection, and aerospace. It is crucial to measure the temperature accurately and reliably at the desired spatial location and time.[1,2] Therefore, a large number of techniques in different modes have proven their feasibility.[3–5] However, there are few methods that can achieve a spatial resolution of less than 10 μm. Luminescent thermometer as a noncontact temperature measurement device with high thermal sensitivity and fast response has irreplaceable advantages in terms of temporal and spatial resolution.[6–8] To date, luminescence phenomenon can be used to detect temperature, which has been explored and developed mainly in terms of emission band position (peak energy), emission bandwidth, intensity, luminescence intensity ratio (LIR), and photoluminescence (PL) decay time.[9–16] Among them, the LIR and emission lifetime techniques are the most exploited selects for luminescence thermometry. Both methods are self-referencing; thus, they can circumvent the adverse effects caused by fluctuations in excitation and electromagnetic compatibility.[17,18] Compared with the lifetime mode, the LIR mode requires less complexity and cost in the instrument composition for temperature detection, but the accuracy of the measurement is poor.[19] Therefore, the shortcoming has inspired researchers to exploit new methods and materials to achieve a more accurate temperature–sensing ability.

There are numerous luminescence materials investigated and utilized as luminescence thermometers, such as polymers, organic dyes, proteins, quantum dots, metal–organic frameworks, as well as transition metal/lanthanide-doped inorganic phosphors.[20–25] Among these materials, inorganic phosphors are one of the most

Y. Chen, G. Li, Y. Ding, Q. Mao, J. Zhong
Center of Advanced Optoelectronic Materials
College of Materials and Environmental Engineering
Hangzhou Dianzi University
Hangzhou 310018, China
E-mail: dingyang@hdu.edu.cn; jiasongzhong@hdu.edu.cn

The ORCID identification number(s) for the author(s) of this article can be found under https://doi.org/10.1002/adpr.202300106.

DOI: 10.1002/adpr.202300106

M. Liu
Department of Chemistry
Zhejiang Sci-Tech University
Hangzhou 310018, China

C. Wang
School of Energy and Environment
City University of Hong Kong
Tat Chee Avenue, Kowloon, Hong Kong 999077, China

R. Zheng, B.-L. Su
Laboratory of Inorganic Materials Chemistry (CMI)
University of Namur
61 rue de Bruxelles, B-5000 Namur, Belgium
E-mail: bao-lian.su@unamur.be

promising luminescent thermometer materials owing to their low toxicity, good physical and chemical stability, and excellent luminescent properties. Different from the extensively reported Mn^{4+} emission-based thermometers, Mn^{2+}-doped materials are rarely applied in luminescent thermometers, even though they have temperature-sensitive emission.[26] Actually, all the luminescence characteristics (like intensity, bandwidth, spectral position, and lifetime) of Mn^{2+} ion are favorable for detecting temperature.[27] This feature caters to the approach of improving the reliability of luminescent thermometers by combining several distinct luminescence parameters with temperature detection capabilities. Therefore, the LIR mode relying on the dual-emission centers of Mn^{2+} and Ln^{3+} can be optimized to achieve a more reliable multiparameter temperature sensing.

For LIR technique, controlling the antithermal quenching of the emission peak as a reference signal is a feasible and effective way to improve the thermal sensitivity. Previous reports confirm that the antithermal quenching performance in the emission of Mn^{4+}, Bi^{3+}, and Pr^{3+} depends strongly on their electron trap states, which can compensate for the loss of luminescence intensity of the nonradiative relaxed carriers under thermal perturbation.[28–30] Moreover, as the phonon energy (or the number of phonons) required for the occurrence of the multiphonon relaxation process during its thermal quenching is larger, Tb^{3+} ion is therefore chosen as the second luminescence center, whose emission is more easily complemented by the thermal activated electrons from defect state with elevating temperature.

On account of the above considerations, an innovative Mn^{2+} and Tb^{3+}-codoped Ca_2LaTaO_6 (CLTO:Mn^{2+}/Tb^{3+}) phosphor with tunable emission of Mn^{2+} and antithermal quenching emission of Tb^{3+} is for the first time developed. The thermal-activated electron compensation between Mn^{2+} and Tb^{3+} is evidenced. By virtue of the deep electron trap states caused by Mn^{2+} dopant in the bandgap of Ca_2LaTaO_6, the electrons in the deep trap can be thermally activated at high temperatures, which can compensate the attenuated Tb^{3+} emission resulting from thermal quenching, thus giving rise to the antithermal quenching effect. This particular luminescent properties facilitate the LIR temperature reading which is dependent on the emission of Mn^{2+} and Tb^{3+}, endowing an extraordinary relative sensitivity S_R of 3.603% K^{-1}. In order to obtain higher sensitivity and reliability, three distinct parameters in the spectra of CLTO:Mn^{2+}/Tb^{3+} samples are extracted to achieve multiparameter temperature sensing using multiple linear regression (MLR) analysis. Accordingly, the outstanding relative thermal sensitivity ranging from 8.72% to 16.11% K^{-1} and temperature uncertainty order of 10^{-3} are reached. These results confirm the significant potential of CLTO:Mn^{2+}/Tb^{3+} for luminescence thermometer application. Moreover, the proposed thermal-activated electron compensation mechanism would inspire more deep studies in exploiting highly advanced phosphors for accurate temperature sensing.

2. Results and Discussion

2.1. Structural and Phase Analysis

The crystal structure of the phosphor has significantly important effects on its optical properties. **Figure 1**a illustrates the powder X-ray diffraction (XRD) patterns of the as-prepared ion-doped Ca_2LaTaO_6 (CLTO) samples. Besides, the XRD patterns of the doped CLTO samples with various ion doping concentrations and categories are shown in Figure S1, Supporting Information. All the diffraction peaks of as-prepared samples match well with the standard card (PDF#73-0083) of CLTO, and no impurity phase is observed. The typical perovskite-type Ca_2LaTaO_6 crystallites belong to the monoclinic phase with the space group $P2_1/n$. As depicted in Figure 1b, Ca1 and Ta1 atoms are located at the centers of [$Ca1O_6$] and [$Ta1O_6$] octahedrons, respectively, while La atoms are situated in the interspace of the octahedrons. From Figure 1c, there are two kinds of Ca sites called [$Ca1O_6$] and [$Ca2La1O_6$] octahedrons, which are connected through corners and edges. According to the principle of similar ion radii and equivalent valence, the Mn^{2+} and Tb^{3+} dopant ions would be inserted in Ca and La sites, respectively.[31,32] Figure 1d–f shows the most intense XRD peak (112) in the 30°–32° range for CLTO:$x$$Mn^{2+}$, CLTO:$y$$Tb^{3+}$, and CLTO:$z$$Mn^{2+}$/5.0%$Tb^{3+}$ samples. It is found that the position of the main peaks of all the samples monotonously shifts to higher angles compared with the reference with increasing doping concentration, indicating the lattice contraction.[31] This result is consistent with the above-noted assumption that smaller Mn^{2+} ($r = 0.83$ Å, CN = 6) and Tb^{3+} ($r = 0.92$ Å, CN = 6) ions replace larger Ca^{2+} ($r = 0.99$ Å, CN = 6) and La^{3+} ($r = 1.05$ Å, CN = 6) ions, respectively. To further validate this assumption, the Rietveld refinements on the XRD data of the representative CLTO:1.0%Mn^{2+}, CLTO:5.0%Tb^{3+}, and CLTO:1.0% Mn^{2+}/5.0%Tb^{3+} phosphors are conducted to obtain detailed information on crystal structures. Figure 1g–i shows all refinement results with low R-factors (Table S1, Supporting Information), indicating the reliability of the refinement results. The cell volumes of CLTO:1.0%Mn^{2+}, CLTO:5.0%Tb^{3+}, and CLTO:1.0%Mn^{2+}/5.0% Tb^{3+} decrease from 272.81 $Å^3$ (ICSD No. 20 916) to 272.36, 272.47, and 272.16 $Å^3$, respectively, implying that the above-noted lattice shrinkage is caused by Tb^{3+} and Mn^{2+} doping.

X-ray photoelectron spectroscopy (XPS) survey spectrum (Figure S2a, Supporting Information) illustrates that the characteristic signals of Ca, La, Ta, O, and Mn elements emerge at the corresponding electron binding energy positions. To check the valance state of Mn dopant, the high-resolution XPS spectrum of Mn 2p is performed. The weak peak of Mn in CLTO is due to the low doping amount. The Mn-2$p_{3/2}$ peak at 641.13 eV and satellite peak at 646.8 eV coincide with the parameters for representing Mn(2$p_{3/2}$) spectra for Mn^{2+} in Mn oxides.[33] Besides, electron paramagnetic resonance (EPR) spectra of CLTO:Mn^{2+} and CLTO:Mn^{4+} are shown in Figure S2c, Supporting Information. The resonance signals exhibit the characteristic of an extended exchange-coupled Mn^{2+} system. Therefore, both XPS and EPR analyses indicate that the valence state of Mn dopant in CLTO is +2.

The morphology of the representative CLTO:Mn^{2+}/Tb^{3+} sample was investigated by scanning electron microscopy (SEM). As shown in Figure S3, Supporting Information, the observed particles exhibiting irregular shapes with sizes of about 50–480 nm (mean size ≈180 nm) are agglomerated together. The high-resolution TEM (HRTEM) images of the CLTO:Mn^{2+}, CLTO:Tb^{3+}, and CLTO:Mn^{2+}/Tb^{3+} samples display the interplanar distances of 4.70, 1.69, and 1.61 Å, respectively, indicating the high crystallinity of these samples (**Figure 2**a).[34,35] The energy-dispersive X-ray spectroscopy (EDX) mapping patterns of the three representative phosphors in Figure 2b demonstrate that the dopant

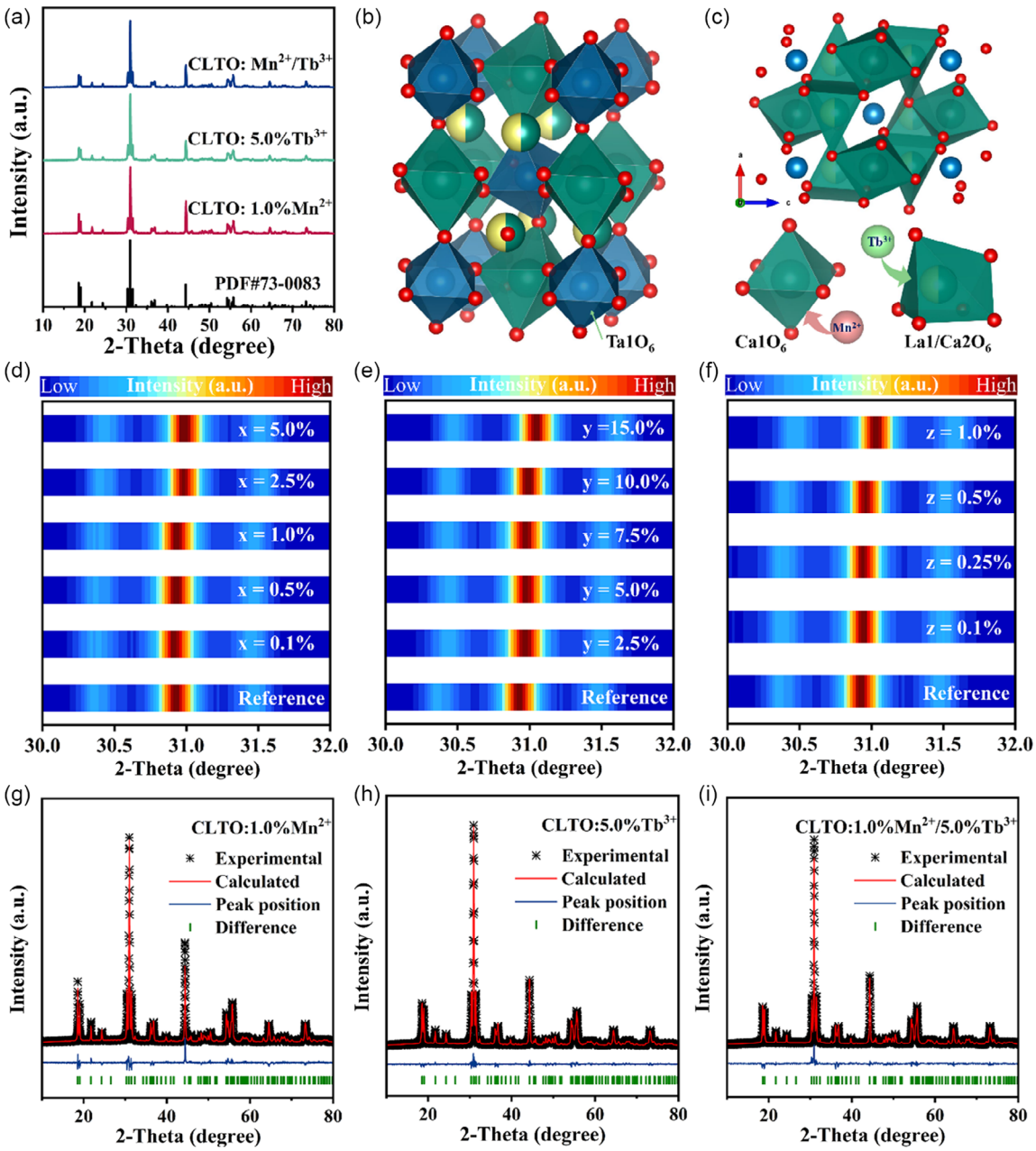

Figure 1. a) XRD patterns of the representative CLTO:1.0%Mn^{2+}, CLTO:5.0%Tb^{3+}, and CLTO:1.0%Mn^{2+}/5.0%Tb^{3+} phosphors. The bottom lines correspond to a standard pattern of CLTO (PDF#73-0083) for comparison. b) Standard orientation of crystal structure for CLTO. c) Views of the corner-sharing or edge-sharing [$Ca1O_6$] and [$La1/Ca2O_6$] octahedrons along the b axis. The main diffraction peak (112) in the 30°–32° range for d) CLTO:xMn^{2+}, e) CLTO:yTb^{3+}, and f) CLTO:zMn^{2+}/5.0%Tb^{3+} samples. The Rietveld refinements of XRD patterns for g) CLTO:1.0%Mn^{2+}, h) CLTO:5.0%Tb^{3+}, and i) CLTO:1.0%Mn^{2+}/5.0%Tb^{3+} phosphors.

elements are homogeneously distributed in the particles, further elucidating the successful introduction of dopant ions (Figure S3, Supporting Information).[36]

2.2. Photoluminescence Properties

The photoluminescence excitation (PLE) and PL spectra of CLTO:1.0%Mn^{2+} sample are shown in Figure S4, Supporting Information. Monitored at 685 nm, the excitation spectrum consists of a charge transfer band (CTB) in the range of 250–300 nm and several very weak narrow peaks corresponding to the spin-forbidden *d–d* transitions of Mn^{2+}. Excited at 270 nm, it is observed that the emission spectrum exhibits a red emission band centered at 685 nm, covering a broad spectral range of 600–800 nm. To investigate the effects of Mn^{2+} doping concentration on emission, the emission spectra of CLTO:xMn^{2+} samples with different dopant concentrations under excitation of 270 nm are investigated and shown in **Figure 3**a.

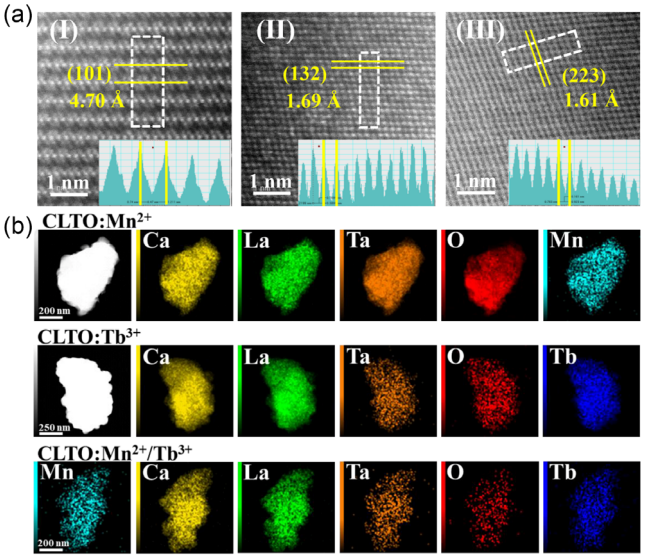

Figure 2. a) HRTEM images and corresponding line analysis of the representative CLTO:Mn^{2+} (I), CLTO:Tb^{3+} (II), and CLTO:Mn^{2+}/Tb^{3+} (III) samples. b) The TEM images with the corresponding element mapping patterns of the as-obtained samples.

When the Mn^{2+} doping concentration over 1.0%, the PL intensities of CLTO:Mn^{2+} samples gradually decrease with enhancing Mn^{2+} doping amounts due to the concentration quenching effect. Significantly, the emission peaks give a slight redshift with increasing Mn^{2+} doping concentration. As shown in Figure 3b, the PL peak position shifts from 680 ($x = 0.1\%$) to 696 nm ($x = 10\%$). According to the Tanabe–Sugano diagram, the low-energy emission band is usually attributed to Mn^{2+} ions undergoing a strong crystal field environment. The crystal field strength (D_q) is mainly dominated by the average bond length (R) between Mn^{2+} and the coordination ions, as shown in Equation (1)[32]

$$D_q \propto \frac{1}{R^5} \tag{1}$$

According to the results obtained in the structural analysis section, the unit cell shrinks with the incorporation of Mn^{2+}. Obviously, the crystal field strength increases so that a longer wavelength emission band occurs.

To obtain more information on the concentration quenching of Mn^{2+} emission, the room-temperature luminescence decay curves of CLTO:$x$$Mn^{2+}$ are measured (Figure 3c). These decay curves can be well fit by a biexponential equation.

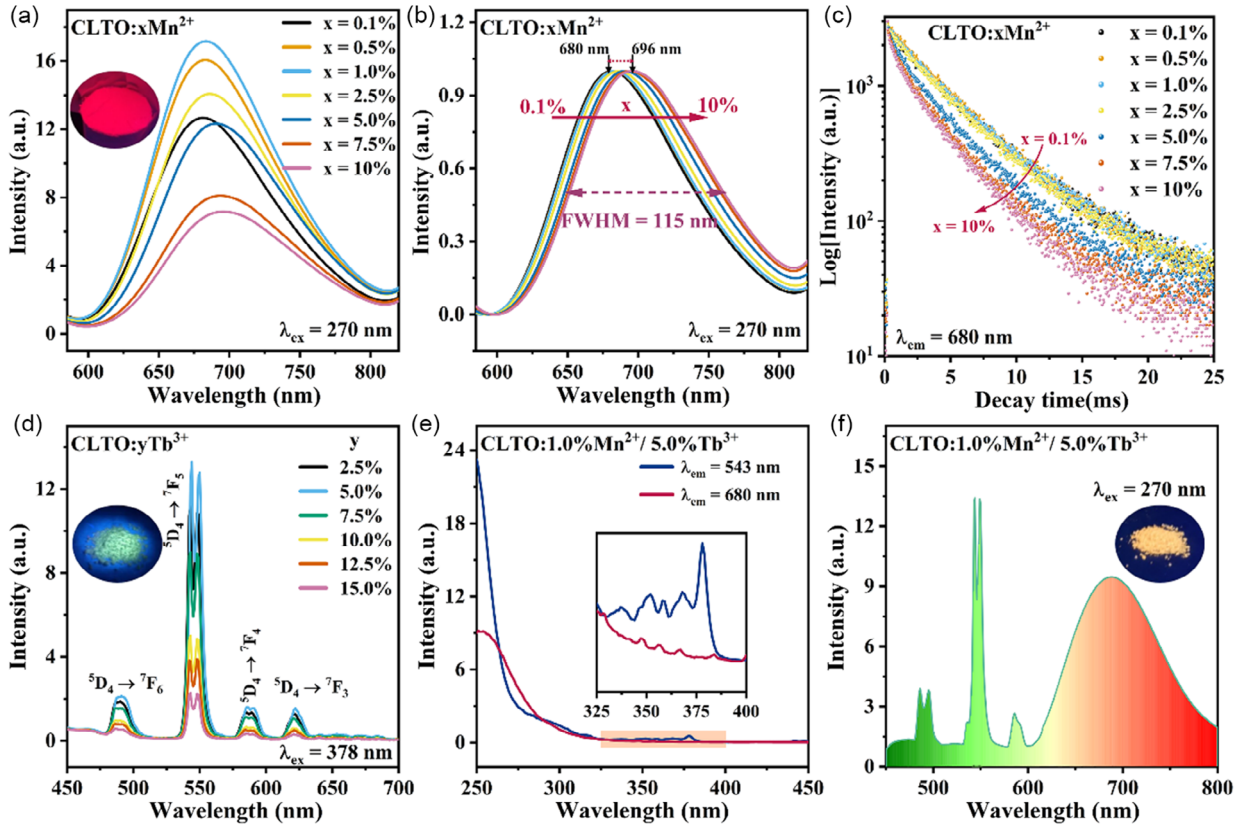

Figure 3. a) Emission spectra and b) normalized emission spectra of CLTO:$x$$Mn^{2+}$ ($x = 0.1\%$–10%) samples excited at 270 nm. c) Luminescence decay curves of CLTO:$x$$Mn^{2+}$ samples monitored at 680 nm. d) Emission spectra of CLTO:yTb^{3+} ($y = 2.5\%$–15%) samples excited at 378 nm. e) Excitation spectra and f) emission spectrum of CLTO:1.0%Mn^{2+}/5.0%Tb^{3+} sample, and the inset show the red highlighted region. (Insets of (a), (d), (f) show the corresponding phosphor photographs under the excitation of UV light).

$$I(t) = A_1 \exp\left(\frac{t}{\tau_1}\right) + A_2 \exp\left(\frac{t}{\tau_2}\right) + I_0 \quad (2)$$

where $I(t)$ and I_0 denote the emission intensities at times t and zero ms, respectively, A_1 and A_2 are constants, and τ_1 and τ_2 represent the lifetimes of rapid and slow decay, respectively. The average lifetimes (τ) can be calculated by the following formula.

$$\tau = \frac{A_1\tau_1^2 + A_2\tau_2^2}{A_1\tau_1 + A_2\tau_2} \quad (3)$$

The details are listed in Table S2, Supporting Information. Clearly, the average lifetimes decrease monotonically with increasing Mn^{2+} doping concentration because of the gradually increasing probability of nonradiative transitions.

Similarly, the emission of Tb^{3+} also exhibits the concentration quenching phenomenon, and the optimal concentration for Tb^{3+} doping is 5.0%. The CLTO:yTb^{3+} phosphors exhibit a series of intense peaks assigned to the transitions from $^5D_4$ to ^7F_J ($J = 6$, 5, 4, 3) under the excitation of 378 nm (Figure 3d). The optimal doping concentrations of Mn^{2+} and Tb^{3+} in the codoped CLTO: Mn^{2+}/Tb^{3+} sample are thus determined to be 1.0% and 5.0%, respectively. The excitation and emission spectra of CLTO:1.0%Mn^{2+}/5.0%Tb^{3+} sample are shown in Figure 3e,f. For the PLE spectrum monitored at 543 nm, the tail of intense band in the range from 250–300 nm is assigned to the 4*f*–5*d* transition and the CTB.[31] The highlighted region in Figure 3e displays several weak peaks centered at 338, 352, 359, 368, and 378 nm, which correspond to the transitions between the $^7F_6$ ground state and $^5L_6$, $^5G_4$, $^5D_2$, $^5G_5$, $^5L_{10}$ states. When monitored at 680 nm, a similar excitation spectrum for single-doped CLTO: Mn^{2+} phosphor (Figure S4a, Supporting Information) is presented. When the CLTO:1.0%Mn^{2+}/5.0%Tb^{3+} sample is under 270 nm excitation (Figure 3f), the broad red emission band of Mn^{2+} can be obviously recognized. However, only the $^5D_4 \rightarrow {}^7F_6$, $^5D_4 \rightarrow {}^7F_5$, and $^5D_4 \rightarrow {}^7F_4$ emission peaks for Tb^{3+} can be found in the spectrum due to the spectral overlap between the emission broadband of Mn^{2+} and the narrow emission for $^5D_4 \rightarrow {}^7F_3$ transition of Tb^{3+}. Moreover, the emission intensities for Mn^{2+} and Tb^{3+} ($^5D_4 \rightarrow {}^7F_5$) are comparable.

To further compare the emission between Tb^{3+} and Mn^{2+}, the emission spectra of CLTO:1.0%Mn^{2+}, CLTO:5.0%Tb^{3+}, and CLTO:1.0%Mn^{2+}/5.0%Tb^{3+} phosphors at different temperatures ranging from 303 to 543 K under 270 nm excitation are shown in **Figure 4**a–c. When the temperature increases from 303 to 543 K, the emission intensity of Mn^{2+} gradually decreases with a slight blueshift of its emission peak position (Figure 4a). This result is ascribed to the lattice expansion caused by the increase in temperature.[17,31] Similar results can be also observed in Figure 4b,c for CLTO:5.0%Tb^{3+} and CLTO:1.0% Mn^{2+}/5.0%Tb^{3+} phosphors, respectively. Figure 4d shows the temperature-dependent integral emission intensity of CLTO:1.0%Mn^{2+} and CLTO: zMn^{2+}/5.0%Tb^{3+} ($z = 0.1\%$, 0.5%, 1.0%). When the temperature increases to 523 K, the integrated intensities remain 20%, 24%, 25%, and 29% of the initial intensities for CLTO:1.0%Mn^{2+}, CLTO: 1.0%Mn^{2+}/5.0%Tb^{3+}, CLTO: 0.5%Mn^{2+}/5.0%Tb^{3+}, and CLTO: 0.1%Mn^{2+}/5.0%Tb^{3+} (at 303 K), respectively. The phenomenon that integral emission decreases with increasing temperature can be found for the above four samples, resulting from the thermal quenching effect. In addition, Figure 4e gives the variation of Tb^{3+} emission integral intensity versus temperature in CLTO: zMn^{2+}/5.0%Tb^{3+} ($z = 0.1\%$, 0.5%, 1.0%). The corresponding temperature-dependent PL spectra are shown in Figure S5, Supporting Information. In CLTO:5.0%Tb^{3+}, the integral intensity of Tb^{3+} emission ($^5D_4$–$^7F_5$) remains almost unchanged at temperatures below 423 K, probably due to the redshift of the CTB tail of its excitation spectrum (Figure S6, Supporting Information), while the emission integral intensity is significantly quenched with temperature over 423 K. Surprisingly, when Mn^{2+} dopant is introduced into the lattice of CLTO:5.0%Tb^{3+}, a clear antithermal quenching phenomenon is observed. Notably, the CLTO:0.5%Mn^{2+}/5.0%Tb^{3+} and CLTO:1.0%Mn^{2+}/5.0%Tb^{3+} phosphors exhibit this antithermal quenching feature over a wide temperature range of 303–523 K.

It is commonly reported that the increase in thermal stability is associated with the presence of defective states.[4] Thermoluminescence (TL) curves for the as-prepared phosphors are examined and depicted in Figure 4f. As shown, no thermal luminescence glow signal is observed for the CLTO:5.0%Tb^{3+} samples. For the CLTO: 0.5%Mn^{2+}/5.0%Tb^{3+} and CLTO: 1.0%Mn^{2+}/5.0%Tb^{3+} samples, two clear and partially overlapped peaks are located in the range of 323–523 K (Figure S7, Supporting Information). It is apparent that the introduction of Mn^{2+} into the CLTO:5.0%Tb^{3+} lattice produces defect states for trapping carriers. The fitted TL curves with two Gaussian peaks (denoted as P1, P2) are shown in Figure 4g. In detail, the P1 peaks of CLTO:0.5%Mn^{2+}/5.0%Tb^{3+} and CLTO:1.0%Mn^{2+}/ 5.0%Tb^{3+} are situated at 385 and 382 K, while that of P2 peaks are located at 473 and 439 K, respectively. The trap depth (E_T) could be determined by the following equation.[29,32]

$$E_T = \frac{T_m}{500} \quad (4)$$

where T_m is the peak temperature of the TL curve (K). The trap depths are calculated to be 0.77 and 0.76 eV for shallow depth (P1), as well as 0.95 and 0.88 eV for deep trap (P2) of CLTO:0.5%Mn^{2+}/5.0%Tb^{3+} and CLTO:1.0%Mn^{2+}/5.0%Tb^{3+}, respectively. As a result, the antithermal quenching of Tb^{3+} emission can be explained as follows (Figure 4h): under the excitation of high-energy UV light (e.g. 270 nm), electrons can be easily excited from the ground state to the excited state or even to the conduction band (CB) at room temperature. At the same time, the defect levels with different depths can effectively trap carriers. As the temperature increases, the excited electrons will be released by nonradiative transitions, and the electrons in the shallow trap will be depopulation by thermal activation. As the temperature increases further, the electrons in the deep trap can also be thermally activated. In other words, the electrons in the trap are continuously released to replenish the Tb^{3+} emission until the temperature rises to 523 K. This eventually leads to the antithermal quenching phenomenon of Tb^{3+} emission, being favorable for the accurate LIR temperature reading, particularly, in high temperatures.

2.3. Luminescent Thermometry

Considering the antithermal quenching phenomenon of Tb^{3+} emission, CLTO:zMn^{2+}/5.0%Tb^{3+} ($z = 0.1\%$, 0.5%, 1.0%) is

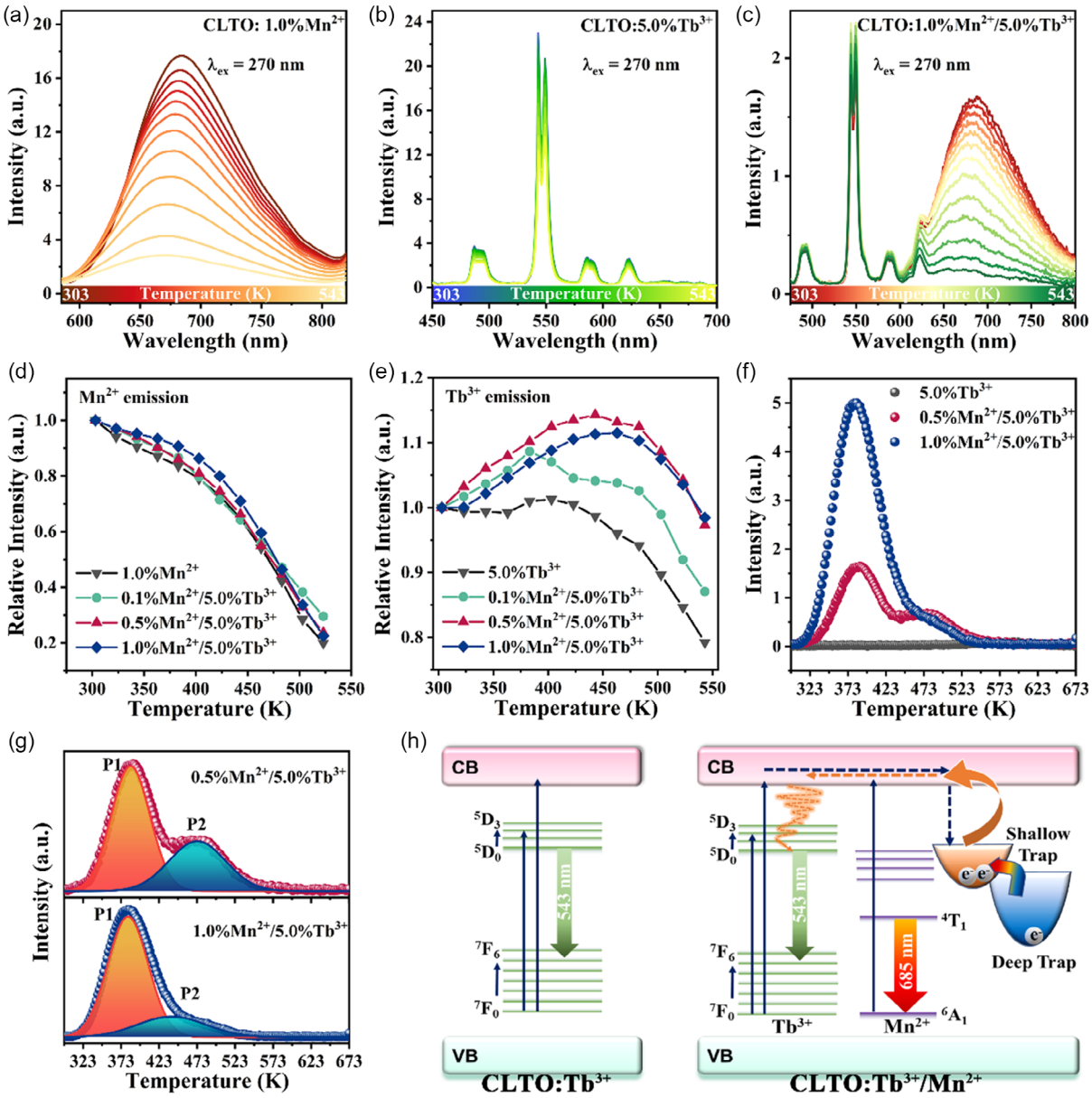

Figure 4. Temperature-dependent emission spectra of a) CLTO:1.0%Mn^{2+}, b) CLTO:5.0%Tb^{3+}, and c) CLTO:1.0%Mn^{2+}/5.0%Tb^{3+} phosphors under 270 nm excitation. d) Integral intensity of Mn^{2+} emission at different temperatures. e) Integral intensity of Tb^{3+} emission ($^5D_4 \rightarrow {}^7F_5$) at different temperatures. f) TL curves of CLTO:5.0%Tb^{3+}, CLTO:0.5%Mn^{2+}/5.0%Tb^{3+}, and CLTO:1.0%Mn^{2+}/5.0%Tb^{3+}. g) The fitted TL curves with two Gaussian peaks of CLTO:0.5% Mn^{2+}/5.0%Tb^{3+} and CLTO:1.0%Mn^{2+}/5.0%Tb^{3+}. h) Schematic illustration of the mechanism for the antithermal quenching process of Tb^{3+} emission.

expected to exhibit great advantages in the LIR temperature sensing. **Figure 5**a presents the thermal evolution of LIR with temperature from 303 to 543 K, which can be calculated according to the following formula.[29]

$$\mathrm{LIR}(T) = \frac{\int_{640}^{800} I_{\mathrm{Mn}}(T)\mathrm{d}\lambda}{\int_{535}^{565} I_{\mathrm{Tb}}(T)\mathrm{d}\lambda} \tag{5}$$

As a result, the LIR value monotonically decreases with increasing temperature, and it can be deduced as the following equation.[30]

$$\mathrm{LIR} = A + B\exp\left(\frac{-\Delta E}{k_{\mathrm{B}}T}\right) \tag{6}$$

where A and B are constants, ΔE is the modified thermal quenching activation energy, and k_{B} is the Boltzmann constant in eV K^{-1}. As the Mn^{2+} concentration decreases from 1.0% to 0.1%, the corresponding fit curves become more linear, and the absolute value of ΔLIR (variation of the LIR in the temperature range of 303–543 K) becomes smaller. Hence, the absolute thermal sensitivity S_A can be obtained as the following formula.[5,9]

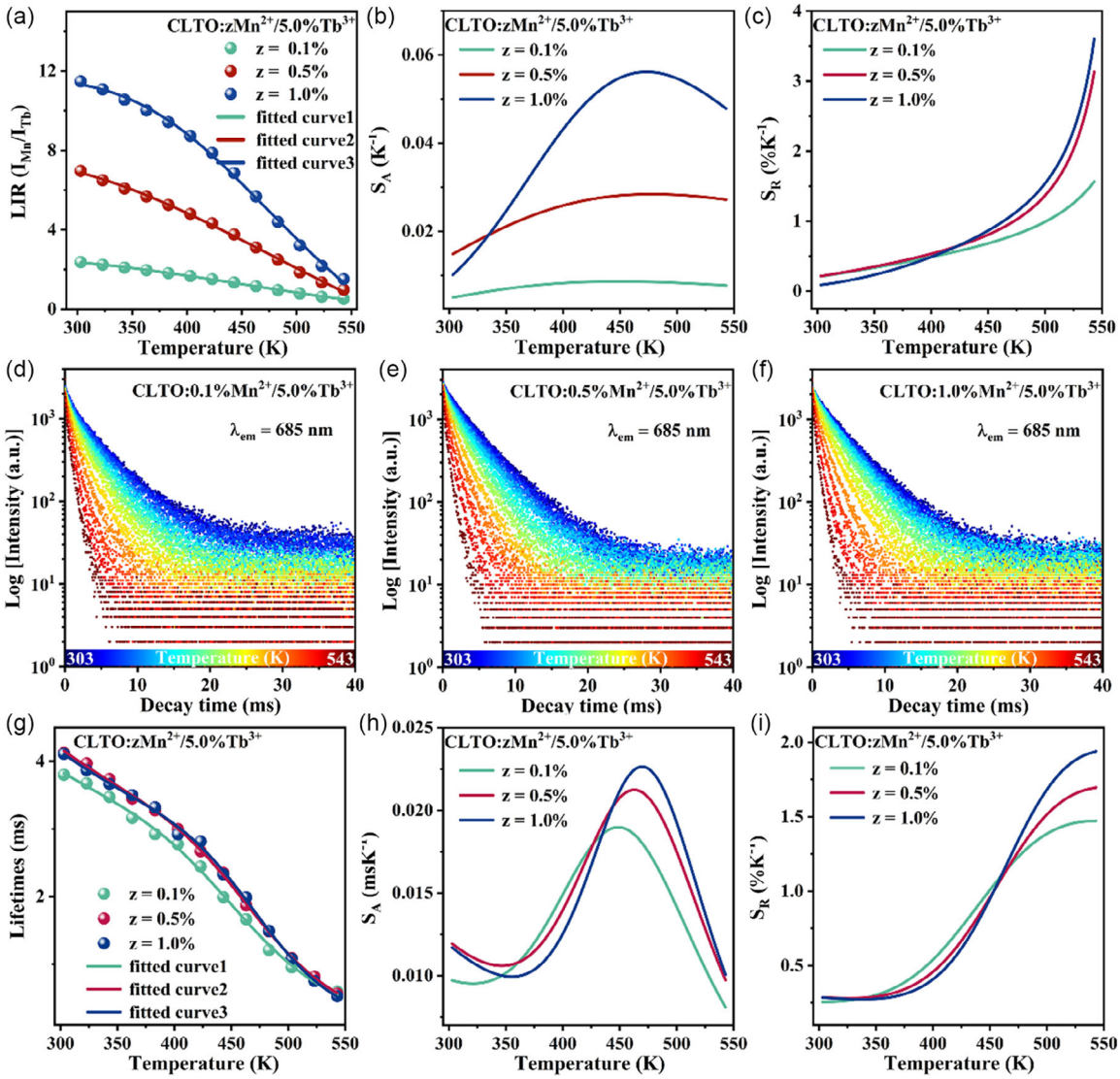

Figure 5. Evolution of a) LIR, b) absolute sensitivity (S_A), and c) relative sensitivity (S_R) with temperature for CLTO:zMn^{2+}/5.0%Tb^{3+} ($z = 0.1\%$, 0.5%, 1.0%) phosphors. d–f) The temperature-dependent decay curves for the as-prepared phosphors. Evolution of g) luminescence lifetimes, h) absolute sensitivity (S_A), and i) relative sensitivity (S_R) of Mn^{2+} emissions in the as-prepared phosphors in the temperature range from 303 to 543 K.

$$S_A = \left|\frac{\mathrm{dLIR}}{\mathrm{d}T}\right| \tag{7}$$

The maximum $S_{Amax} = 0.056\ K^{-1}$(@473 K) in CLTO:1.0% Mn^{2+}/5.0%Tb^{3+} appears, and all absolute thermal sensitivity curves increase and then decrease with increasing temperature (Figure 5b). The absolute sensitivity is almost equal to a constant over the whole temperature range when the Mn^{2+} concentration is 0.1%. To further evaluate the performance of this LIR temperature reading, the thermometric parameter called relative thermal sensitivity (S_R) is calculated as follows.[5,9]

$$S_R = \left|\frac{\mathrm{dLIR}}{dT}\right| \frac{1}{\mathrm{LIR}} \cdot 100\% \tag{8}$$

The calculated values and corresponding curves are shown in Figure 5c. Likewise, the maximum value of the relative thermal sensitivity $S_{Rmax} = 3.603\%\ K^{-1}$(@543 K) is also presented in CLTO:1.0%Mn^{2+}/5.0%Tb^{3+}. Notably, the values of S_R are very close for both CLTO:0.5%Mn^{2+}/5.0%Tb^{3+} and CLTO:1.0% Mn^{2+}/5.0%Tb^{3+} at each temperature due to the similar antithermal quenching curves of the Tb^{3+} emission in both samples. The optimal CLTO:1.0%Mn^{2+}/5.0%Tb^{3+} phosphor with outstanding thermal sensitivity demonstrates that such unique antithermal quenching behavior is quite favorable for the LIR temperature reading.

Besides LIR temperature readout, CLTO:zMn^{2+}/5.0%Tb^{3+} ($z = 0.1\%$, 0.5%, 1.0%) is found to be able to detect temperature using the emission lifetime of Mn^{2+}. Temperature-dependent PL decay curves of Mn^{2+} and Tb^{3+} in CLTO:zMn^{2+}/5.0%Tb^{3+}

samples are given in Figure 5d–f and S8, Supporting Information. As presented, the decay curves of all samples decay fast with increasing temperature. Consistently, the emission lifetimes calculated according to Equation (2) and Equation (3) are found to exhibit a monotonic decrease with increasing temperature due to the increased probability of nonradiative transition process. Their lifetimes as a function of temperatures are described by the following equation.[17,19]

$$\tau(T) = \frac{\tau_R(0)\cdot \tanh\left(\frac{h\nu}{2k_BT}\right)}{1+\left(\tau_R(0)\cdot \tanh\left(\frac{h\nu}{2k_BT}\right)\Big/\tau_{NR}\right)\cdot\exp(-\Delta E_{Mn}/k_BT)} \quad (9)$$

Where $\tau_R(0)$ is the radiative lifetime at $T = 0$ K, k_B is the Boltzmann constant in $cm^{-1}\,K^{-1}$, $h\nu$ is the average energy of phonons coupled to the $^4T_1 \rightarrow {}^6A_1$ transition, $1/\tau_{NR}$ is the nonradiative decay rate, and ΔE_{Mn} is the activation energy of the process. As illustrated in Figure 5g, the fitted curve of CLTO:1.0%Mn^{2+}/5.0%Tb^{3+} almost coincides with that of CLTO:0.5%Mn^{2+}/5.0%Tb^{3+}, being slightly different with that of CLTO:0.1%Mn^{2+}/5.0%Tb^{3+}. To assess the performance, the absolute (S_a) and relative (S_r) thermal sensitivities are calculated as follows.[17]

$$S_A = \left|\frac{d\tau}{dT}\right| \quad (10)$$

$$S_R = \frac{1}{\tau}\left|\frac{d\tau}{dT}\right| \times 100\% \quad (11)$$

Figure 5h,i shows that the highest absolute and relative thermal sensitivities are observed in the CLTO:1.0%Mn^{2+}/5.0%Tb^{3+} sample with maximum values of $S_{Amax} = 0.023\ K^{-1}$ (@470 K) and $S_{Rmax} = 1.941\%\ K^{-1}$ (@543 K), respectively. Furthermore, it can be recognized in the temperature-dependent absolute and relative thermal sensitivity curves that the relationship between the values near 400 K and Mn^{2+} concentration is opposite to that near 500 K. This result may be attributed to the difference in the phonon energy coupled to the electron radiative transition in the host.

Moreover, the temperature uncertainty (δT) is a thermometric parameter to assess the accuracy of the designed thermometer, which is given by[18,19]

$$\delta T = \frac{1}{S_R}\frac{\delta\Delta}{\Delta} \quad (12)$$

where $\delta\Delta/\Delta$ is the relative error in the determination of the thermometric parameter ($\delta\Delta$ can be determined as a standard deviation in 30 measurements at a certain temperature, as shown in Figure S9, Supporting Information). The temperature uncertainties δT_{LIR} of the LIR temperature readings are higher than 0.067, 0.021, and 0.011 K for CLTO:0.1%Mn^{2+}/5.0%Tb^{3+} CLTO:0.5%Mn^{2+}/5.0%Tb^{3+}, and CLTO:1.0%Mn^{2+}/5.0%Tb^{3+}, respectively. The maximum uncertainty is up to 0.117 K at 303 K for CLTO:0.1%Mn^{2+}/5.0%Tb^{3+}. The temperature uncertainty $\delta T_{lifetime}$ of all lifetime-based thermometers is almost below 0.015 K and is as low as 10^{-3} orders of magnitude in the temperature range of 423 to 523 K.

Although the lifetime-based temperature measurement method has a much lower thermal sensitivity than that of LIR method, it has a significant advantage in terms of temperature uncertainty. In order to obtain more accurate temperature measurement results without sacrificing sensitivity, a novel multiparameter temperature-sensing mode is designed. The relative weights of the full width at half maximum (FWHM), peak energy, and LIR considered by MLR are depicted in **Figure 6**a. We combine multiple temperature-sensitive parameters in the emission spectrum of Mn^{2+} with the earlier-mentioned LIR temperature measurement mode in a reasonable way. Figure 6b presents the temperature-dependent emission spectrum of CLTO:0.5%Mn^{2+}/5.0%Tb^{3+} in the temperature range of 303–443 K. The peak energies and FWHM of Mn^{2+} emission band and LIR parameters serve as independent variables for multiparameter temperature sensing, which can be extracted from this spectrum as a function of temperature, as plotted in Figure 6c–e. Clearly, the dependence of all luminescence parameters on temperature can be described by a linear fitting. These three reliable methods can measure temperature independently and have the maximum relative sensitivities of 0.13, 0.73, and 0.62% K^{-1}, respectively.

Furthermore, the data of three luminescence parameters were treated by MLR analysis. The temperature could then be expressed as a function of each parameter (Δ_1, Δ_2, Δ_3)[25]

$$T = \beta_0 + \beta_1\Delta_1 + \beta_2\Delta_2 + \beta_3\Delta_3 + \varepsilon \quad (13)$$

where β_0 is the intercept, β_i ($i = 1, 2, 3$) is the slope of each thermometric parameter Δ_i (Δ_1, Δ_2, and Δ_3 represent FWHM, peak energy, and LIR, respectively.), and $\boldsymbol{\epsilon}$ is the residual. Hence, the expression for the relative sensitivity S_R and the temperature uncertainty δT can be rewritten as follows.[25]

$$S_R = \sqrt{\sum_{i=1}^{n}\left(\frac{1}{\Delta_i}\left|\frac{d\Delta_i}{dT}\right|\right)^2} = \sqrt{\sum_{i=1}^{n}(\Delta_i\beta_i)^{-2}} \quad (14)$$

$$\delta T = \frac{1}{S_R}\sqrt{\sum_{i=1}^{n}\left(\frac{\delta\Delta_i}{\Delta_i}\right)^2} \quad (15)$$

As shown in Figure 6f, the calculated temperatures from the MLR agree well with the temperatures measured by the thermocouples, indicating that the method provides highly reliable temperature readings. Notably, compared with the LIR method, a significant improvement in sensitivity over the entire measurement temperature range was observed in the multiparameter temperature sensing through MLR. When the temperature rises from 303 to 443 K, the sensitivity increases from 8.72% to 16.11% K^{-1} (Figure 6g). More importantly, the temperature uncertainty in the temperature range of 303–443 K reduces to the order of 10^{-3} (Figure 6h), which provides a better δT than the lifetime-based thermometer. Such excellent temperature measurement results demonstrate the high advantages and feasibility of CLTO:Mn^{2+}/Tb^{3+} for multiparameter sensing applications and provide a new approach to develop more reliable and sensitive luminescence thermometers.

Finally, we have compared our results with related phosphors that have been reported in previous literature, and the temperature-sensing performance of our reported Ca_2LaTaO_6:Mn^{2+}/Tb^{3+} phosphor surpasses most of the reported phosphor based thermometers to date (see **Table 1**), further demonstrating the

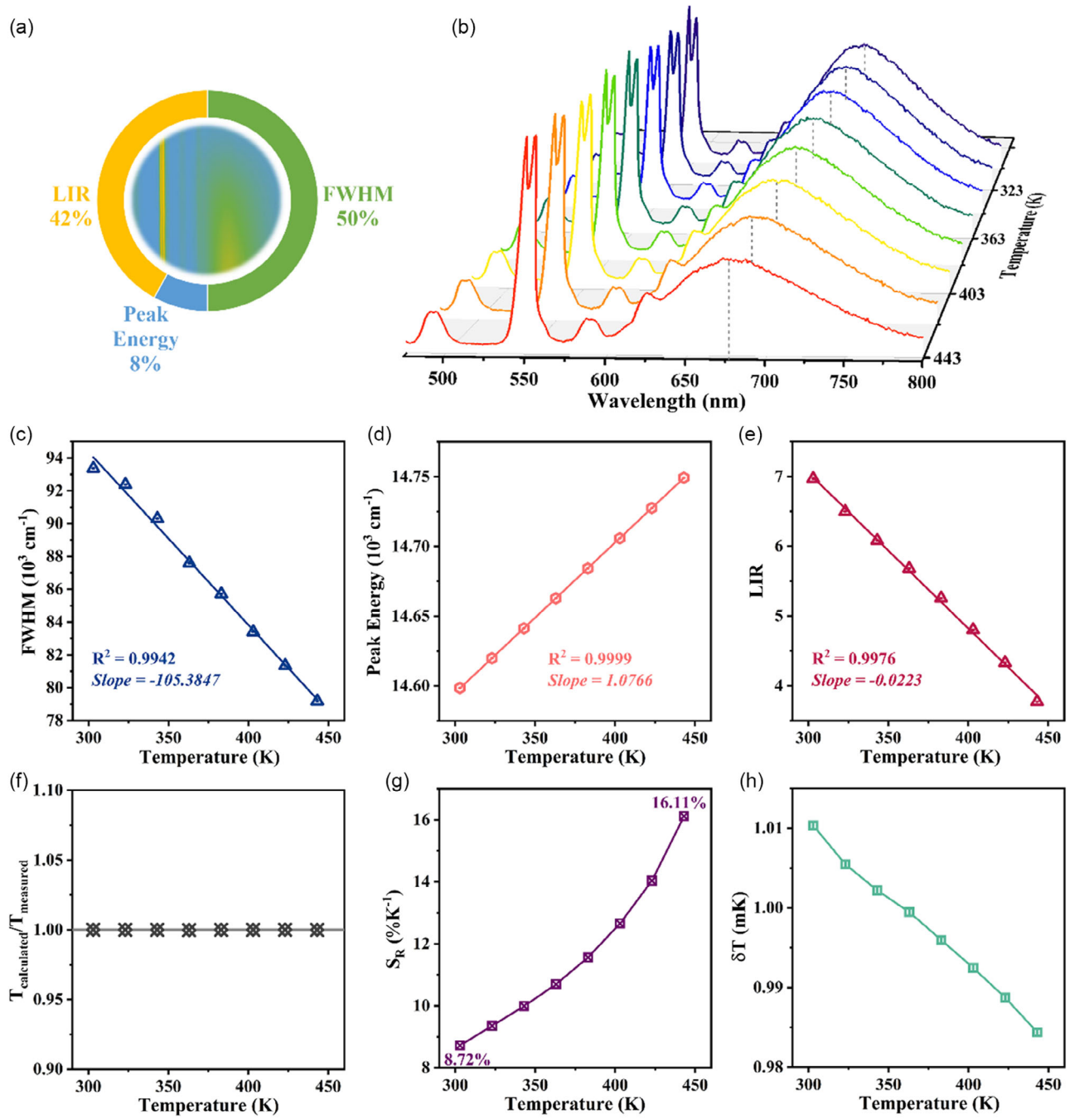

Figure 6. a) Donut chart of the relative weights of the FWHM, peak energy, and LIR considered by MLR. b) Temperature-dependent emission spectra of CLTO:0.5%Mn^{2+}/5.0%Tb^{3+} phosphors under 270 nm excitation. c–e) Temperature dependence of FWHM, peak energy, and LIR. The lines are the best linear fits of the corresponding data. f) The ratio of the temperature calculated from the multiparameters sensing through MLR to the temperature measured by the thermocouple. g) Relative thermal sensitivity and h) temperature uncertainty of the multiparameters sensing through MLR.

superior temperature-sensing ability of the obtained antithermal quenching phosphors.

3. Conclusion

In summary, an innovative Mn^{2+} and Tb^{3+}-codoped Ca_2LaTaO_6 phosphor with tunable emission of Mn^{2+} and antithermal quenching emission of Tb^{3+} is prepared. This unique luminescence phenomenon is attributed to the complementation of thermal-activated electrons at the defect states, which can release electrons by thermal activation to replenish the Tb^{3+} emission. The feasibility of the CLTO:Mn^{2+}/Tb^{3+} phosphors for multiple temperature reading using LIR, emission lifetimes, and distinct luminescence parameters is explored and demonstrated. It is

Table 1. Comparison of temperature-sensing performances for phosphor-based thermometer.

Phosphor	Temperature sensing	Relative sensitivity [%K^{-1} K]	δT [K]	Ref.
$BaLaCa_{0.1}Mg_{0.9}SbO_6:Mn^{4+}$	Lifetime	1.42 (488)	0.009	[12]
$Mg_3Y_{2(1-y)}Ge_3O_{12}:Mn^{4+}$	LIR	0.019 (300)	N/A	[28]
$Li_2Zn_{0.85}SiO_4:Mn^{2+}$	LIR	0.848 (373)	N/A	[37]
$Sc_2O_3:Eu^{2+}/Eu^{3+}$	LIR	3.06 (267)	N/A	[38]
$COF:Eu^{3+}/Tb^{3+}$	LIR	1.403 (150)	0.05	[39]
$YAlO_3:Yb^{3+},Er^{3+},Mn^{4+}$	LIR	1.95 (530)	N/A	[40]
$Sr_4Al_{14}O_{25}:Mn^{4+},Tb^{3+}$	LIR	2.8 (423)	0.02	[41]
$Ca_2LaTaO_6:Mn^{2+}/Tb^{3+}$	LIR	3.603 (543)	0.001	This work

concluded that the CLTO:1.0%Mn^{2+}/5.0%Tb^{3+} provides the maximum relative thermal sensitivity S_R of 3.603% K^{-1} via the LIR approach with the help of Tb^{3+} antithermal quenching emission. The lifetime-based luminescent thermometer on CLTO: Mn^{2+}/Tb^{3+} reveals S_R of 1.941% K^{-1} at 543 K. Multiparametric temperature sensing using MLR is achieved by combining three independently and linearly temperature-dependent luminescence parameters to obtain excellent thermometer performance with relative thermal sensitivity ranging from 8.72% to 16.11% K^{-1}. Besides, the temperature uncertainty is of the order of 10^{-3}. All of these results support that CLTO: Mn^{2+}/Tb^{3+} is one of the most promising thermal-sensing candidates and provides a new strategy to design and optimize more reliable and sensitive luminescence thermometers.

4. Experimental Section

Preparation of Phosphor Materials: The phosphor materials were synthesized by a molten salt method. First, $CaCO_3$ (99.95%, Aladdin), La_2O_3 (99.99% Aladdin), Ta_2O_5 (99.99%, Aladdin), Tb_4O_7(99.99%, Aladdin), and $MnCO_3$ (99.99%, Aladdin) were weighed according to the stoichiometric composition of $Ca_2LaTaO_6:xMn^{2+}$($x = 0.1\%$, 0.5%, 1.0%, 2.5%, 5%, 7.5%, and 10%), $Ca_2LaTaO_6:yTb^{3+}$($y = 2.5\%$, 5.0%, 7.5%, 10%, 12.5%, and 15%), and $Ca_2LaTaO_6:zMn^{2+}/5\%Tb^{3+}$($z = 0.1\%$, 0.25%, 0.5%, and 1.0%). The NaCl (99.9%, Aladdin) as the molten salt with a salt-to-material ratio of 1:3 was then added and ground in an agate mortar for 30 min. After being ground thoroughly, the mixed powders were transferred into an alumina crucible, preheated at 800 °C for 6 h, and subsequently sintered at 1000 °C for 6 h under reducing atmosphere (5 vol% H_2 + 95 vol% N_2, 99.999%) in a tube furnace. After cooling down to room temperature naturally, the prepared powders were reground into fine target phosphors. For the preparation of $Ca_2LaTaO_6:Mn^{4+}$, the same method was used except for calcination under air atmosphere.

Characterization: The crystal structures of the prepared samples were characterized by an X-ray powder diffraction (XRD, Rigaku MiniFlex 600 X-ray diffractometer) device employing a Cu target Kα radiation source ($\lambda = 1.54056$ Å). The scanning mode for the as-prepared samples was conducted at a diffraction angle range of 10°–80° with a scan rate of 2° min^{-1} under an operation of 40 kV and 15 mA. Rietveld refinement was performed using the General Structural Analysis System (GSAS) program. The morphology observation and elemental composition analysis of the samples were carried out by SEM (FEI ApreoHiVac) equipped with an X-ray energy-dispersive spectrometer (EDS). Emission spectra (PL), excitation spectra (PLE), and fluorescence decay curves were measured at room temperature using an FS5 fluorescence spectrometer (Edinburgh Instruments) with a 150 W continuous excitation xenon lamp and a pulsed light source. Temperature-dependent emission spectra and decay curves in the range from 303 to 503 K were detected on the same spectrophotometer equipped with a computer-controlled electric heater. XPS was performed on a Thermo ESCALAB 250XI. TL spectrum was performed in a TOSL-3DS TL 3D spectrometer (Rongfan, Guangzhou), using X-rays as the excitation light source.

Supporting Information

Supporting Information is available from the Wiley Online Library or from the author.

Acknowledgements

Y.C. and G.L. contributed equally to this work. This work was supported by the National Natural Science Foundation of China (52072101 and 51972088) and the Fundamental Research Funds for the Provincial Universities of Zhejiang (GK229909299001-003).

Conflict of Interest

The authors declare no conflict of interest.

Data Availability Statement

The data that support the findings of this study are available in the supplementary material of this article.

Keywords

broadbands, lifetime-based thermometers, luminescence intensity ratios, multiparametric readouts, tunable emission

Received: March 17, 2023
Published online: April 14, 2023

[1] G. Kucsko, P. C. Maurer, N. Y. Yao, M. Kubo, H. J. Noh, P. K. Lo, H. Park, M. D. Lukin, *Nature* **2013**, *500* 54.
[2] L. Liang, X. Liu, *Nat. Photonics* **2018**, *12* 124.
[3] J. Zhou, B. del Rosal, D. Jaque, S. Uchiyama, D. Jin, *Nat. Methods* **2020**, *17* 967.
[4] B. Zhao, Y. Chen, Y. Xue, Q. Mao, G. Bai, M. Liu, J. Zhong, *Mater. Des.* **2023**, *227*, 111802.
[5] J. Zhong, D. Chen, Y. Peng, Y. Lu, X. Chen, X. Li, Z. Ji, *J. Alloys Compd.* **2018**, *763*, 34.
[6] A. R. N. Bastos, C. D. S. Brites, P. A. Rojas-Gutierrez, C. DeWolf, R. A. S. Ferreira, J. A. Capobianco, L. D. Carlos, *Adv. Funct. Mater.* **2019**, *29*, 1905474.
[7] P. Du, X. Huang, J. S. Yu, *Inorg. Chem. Front.* **2017**, *4*, 1987.
[8] Z. Zhang, Y. Wu, H. Suo, X. Zhao, C. Guo, *Mater. Res. Bull.* **2021**, *133*, 111079.
[9] L. Shi, W. Song, C. Lian, W. Chen, J. Mei, J. Su, H. Liu, H. Tian, *Adv. Opt. Mater.* **2018**, *6*, 1800190.
[10] J. Wang, H. Lin, Y. Cheng, X. Cui, Y. Gao, Z. Ji, J. Xu, Y. Wang, *Sens. Actuator B Chem.* **2019**, *278*, 165.
[11] S. Liang, G. Li, P. Dang, Y. Wei, H. Lian, J. Lin, *Adv. Opt. Mater.* **2019**, *7*, 1900093.

[12] G. Li, G. Li, Q. Mao, L. Pei, H. Yu, M. Liu, L. Chu, J. Zhong, *Chem. Eng. J.* **2022**, *430*, 132923.
[13] D. K. Amarasinghe, F. A. Rabuffetti, *Chem. Mater.* **2019**, *31*, 10197.
[14] Y. Shen, H. D. A. Santos, E. C. Ximendes, J. Lifante, A. Sanz-Portilla, L. Monge, N. Fernández, I. Chaves-Coira, C. Jacinto, C. D. S. Brites, L. D. Carlos, A. Benayas, M. C. Iglesias-de la Cruz, D. Jaque, *Adv. Funct. Mater.* **2020**, *30*, 2002730.
[15] Y. Gao, F. Huang, H. Lin, J. Zhou, J. Xu, Y. Wang, *Adv. Funct. Mater.* **2016**, *26*, 3139.
[16] J. Drabik, L. Marciniak, *ACS Appl. Mater. Interfaces* **2021**, *13*, 1261.
[17] W. M. Piotrowski, K. Trejgis, M. Dramicanin, L. Marciniak, *J. Mater. Chem. C* **2021**, *9*, 10309.
[18] L. Marciniak, W. Piotrowski, M. Szalkowski, V. Kinzhybalo, M. Drozd, M. Dramicanin, A. Bednarkiewicz, *Chem. Eng. J.* **2022**, *427*, 131941.
[19] K. Trejgis, M. D. Dramićanin, L. Marciniak, *J. Alloys Compd.* **2021**, *875*, 159973.
[20] V. Trannoy, A. N. C. Neto, C. D. S. Brites, L. D. Carlos, H. Serier-Brault, *Adv. Opt. Mater.* **2021**, *9* 2001938.
[21] H. Cai, W. Lu, C. Yang, M. Zhang, M. Li, C.-M. Che, D. Li, *Adv. Opt. Mater.* **2019**, *7*, 1801149.
[22] X. Qiu, Q. Zhou, X. Zhu, Z. Wu, W. Feng, F. Li, *Nat. Commun.* **2020**, *11*, 4.
[23] H. Zhang, Y. Liang, H. Yang, S. Liu, H. Li, Y. Gong, Y. Chen, G. Li, *Inorg. Chem.* **2020**, *59*, 14337.
[24] S. Uchiyama, N. Kawai, A. P. de Silva, K. Iwai, *J. Am. Chem. Soc.* **2004**, *126*, 3032.
[25] F. E. Maturi, C. D. S. Brites, E. C. Ximendes, C. Mills, B. Olsen, D. Jaque, S. J. L. Ribeiro, L. D. Carlos, *Laser Photonics Rev.* **2021**, *15*, 2100301.
[26] X. Yang, C. Pu, H. Qin, S. Liu, Z. Xu, X. Peng, *J. Am. Chem. Soc.* **2019**, *141* 2288.
[27] Y. Fu, C. Li, F. Zhang, S. Huang, Z. Wu, Y. Wang, Z. Zhang, *Chem. Eng. J.* **2021**, *409*, 128190.
[28] Y. Wei, H. Yang, Z. Gao, Y. Liu, G. Xing, P. Dang, A. A. A. Kheraif, G. Li, J. Lin, R.-S. Liu, *Adv. Sci.* **2020**, *7*, 1903060.
[29] L. Wu, S. Sun, Y. Bai, Z. Xia, L. Wu, H. Chen, L. Zheng, H. Yi, T. Sun, Y. Kong, Y. Zhang, J. Xu, *Adv. Opt. Mater.* **2021**, *9*, 2100870.
[30] W. Ye, C. Ma, Y. Li, C. Zhao, Y. Wang, C. Zuo, Z. Wen, Y. Li, X. Yuan, Y. Cao, *J. Mater. Chem. C* **2021**, *9*, 15201.
[31] K. Ueda, S. Tanaka, R. Yamamoto, Y. Shimizu, T. Honma, F. Massuyeau, S. Jobic, *J. Phys. Chem. C* **2020**, *124*, 854.
[32] E. Song, J. Wang, S. Ye, X.-B. Yang, M. Peng, Q. Zhang, L. Wondraczek, *Adv. Opt. Mater.* **2017**, *5*, 1700070.
[33] H. W. Nesbitt, D. Banerjee, *Am. Mineral.* **1998**, *83*, 305.
[34] M. H. Sun, J. Zhou, Z. Y. Hu, L. H. Chen, L. Y. Li, Y. D. Wang, B. L. Su, *Matter* **2020**, *3*, 1226.
[35] L. Wu, Y. Li, Z. Y. Fu, B. L. Su, *Natl. Sci. Rev.* **2020**, *7*, 1667.
[36] X. Zheng, G. Shen, C. Wang, Y. Li, D. Dunphy, T. Hasan, B. L. Su, *Nat. Commun.* **2017**, *8*, 14921.
[37] E. Song, M. Chen, Z. Chen, Y. Zhou, W. Zhou, H. T. Sun, Q. Zhang, *Nat. Commun.* **2022**, *13*, 2166.
[38] Y. Pan, X. Xie, Q. Huang, C. Gao, Y. Wang, L. Wang, W. Huang, *Adv. Mater.* **2018**, *30*, 1705256.
[39] A. M. Kaczmarek, Y. Y. Liu, M. K. Kaczmarek, H. Liu, F. Artizzu, L. D. Carlos, P. Van Der Voort, *Angew. Chem., Int. Ed.* **2020**, *132*, 1948.
[40] D. Chen, W. Xu, S. Yuan, X. Li, J. Zhong, *J. Mater. Chem. C* **2017**, *5*, 9619.
[41] W. Piotrowski, K. Trejgis, K. Maciejewska, K. Ledwa, B. Fond, L. Marciniak, *ACS Appl. Mater. Interfaces* **2020**, *12*, 44039.